Supplemental Document

Biomedical Optics EXPRESS

Heterodyne Brillouin microscopy for biomechanical imaging: supplement

MICHAEL A. TAYLOR,* AMANDA W. KIJAS, ZHAO WANG, JAN LAUKO, AND ALAN E. ROWAN

Australian Institute for Bioengineering and Nanotechnology, The University of Queensland, St. Lucia, Queensland 4072, Australia
**m.taylor@sbs.uq.edu.au*

Supplement DOI: https://doi.org/10.6084/m9.figshare.16556220

Parent Article DOI: https://doi.org/10.1364/BOE.435869

Heterodyne Brillouin microscopy for biomechanical imaging: supplemental document

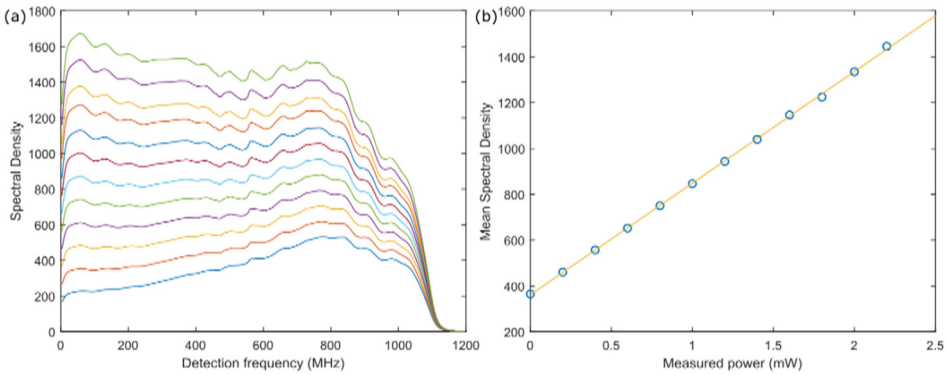

Fig. S1: Noise performance of detector. (a) Spectrum of the detector output as the reference power increases from 0 mW to 2.2 mW. Spectral Density is in arbitrary units. The lowest spectrum includes no light and corresponds to the detector noise. Digitizer noise is far smaller and not visible on this plot scale. The addition of laser power should contribute spectrally flat shot noise, therefore the variations with frequency indicates variations in detection sensitivity across the measurement bandwidth. (b) Averaged spectral density below 1000 MHz, showing a linear increase over the range 0 mW to 2.1 mW, after which the detectors begin to saturate. The constant offset is due to the electronic detector noise. The linear increase is the signature of shot noise, and confirms the detection to be limited by shot noise above 0.8 mW. The experiments used 1.6 mW of reference power, at which shot noise is more than double the electronic noise floor.

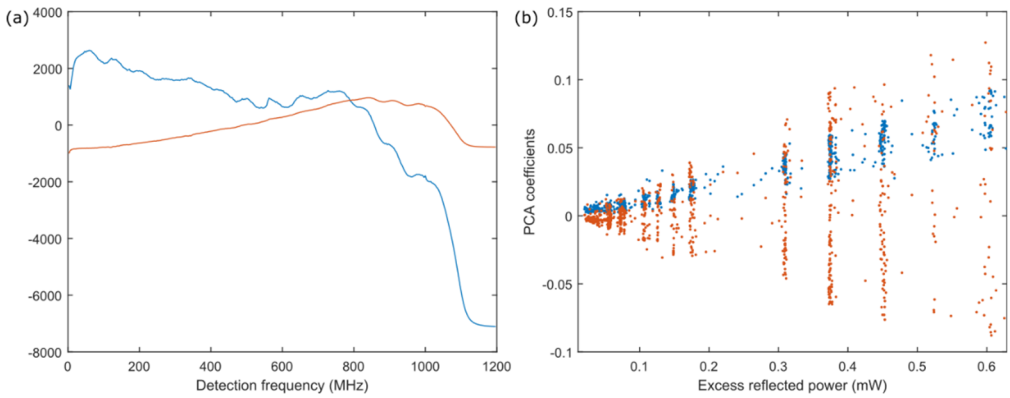

Fig. S2: Quantification of noise due to stray light. Spectra were measured while varying amount of reflected light was inserted into the signal port of the microscope. Principal component analysis (PCA) was used on the resulting set of spectra to identify how the excess power influences the detection. (a) The first two principal components, which collectively account for 99.9 % of the variations in the measured spectra. This means that changes the in spectral shape due to stray light can be well approximated as a linear sum of the two principal component spectra. The first principal component (blue) approximately matches the variations in detection sensitivity across the measurement bandwidth (Fig. S1a), and the second component (orange) approximates a linear ramp over the detection bandwidth. (b) The coefficients of each principal component, as a function of the excess power. The first principal component (blue) coefficient increases approximately linearly with the extra power, suggesting it is primarily caused by additional shot noise. The second component (orange) coefficient becomes increasingly variable with extra power, but no change in mean. This is consistent with excess laser noise, which can change in sign due to uncontrolled shifts in the phase between the reference and reflected light. These components provide excess background noise when imaging scattering samples, and the shot noise is subtracted from spectra when processing data. In pure liquids these components are not observable.

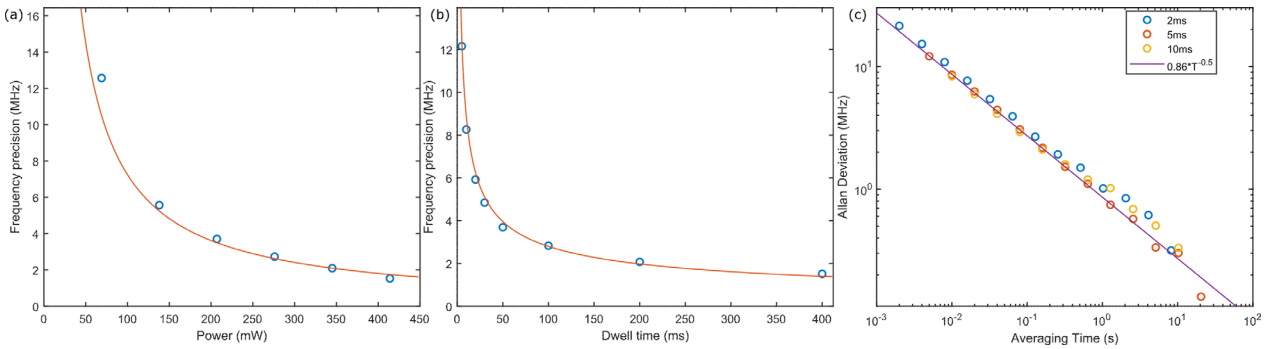

Fig. S3: Precision of the heterodyne measurements of Brillouin scattering in water, with precision Δν defined as the standard deviation of Brillouin peak frequencies estimated from a sequence of measured spectra. (a) Change in precision with probe power, measured with 200 ms pixel dwell. The fit shows a $\Delta\nu \propto P^{-1}$ dependence on the power P. (b) Measured precision with differing dwell times, ranging from 2 ms to 400 ms, and measured with 345 mW. The fit follows $\Delta\nu \propto T^{-1/2}$ with the averaging time T. The dependence is predicted in Eq. (28). (c) Allan variance of series of measurements, recorded with pixel dwell times of 2 ms (blue), 5 ms (orange), and 10 ms (yellow). The Allan variance converges to 0.86 $T^{-1/2}$ for longer dwell times, with a slight reduction in precision for the shortest 2ms dwell.

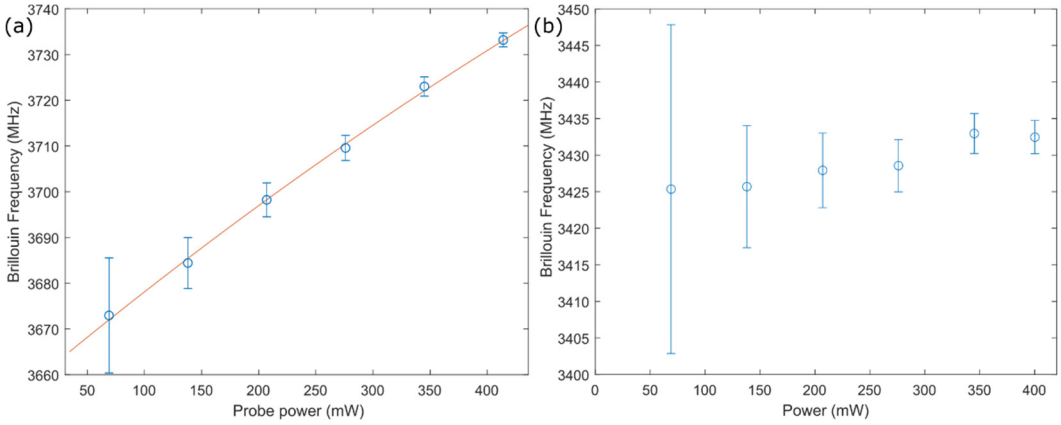

Fig. S4: Laser heating. (a) The Brillouin shift of water increases as the input laser power is increased, consistent with the expected change in Brillouin frequency as the temperature increases. Error bars denote the standard deviation of a sequence of measurements. The fit represents the expected Brillouin frequency shift if the rate of laser heating is held constant at 27.5 K/W. (b) The Brillouin shift in heavy water D_2O is 240-300 MHz lower than in water. The change in Brillouin shift in heavy water with laser power is approximately 10 times smaller than in water, suggestive of less than 3 K/W heating. The residual heating in heavy water may be due to contamination with regular water.

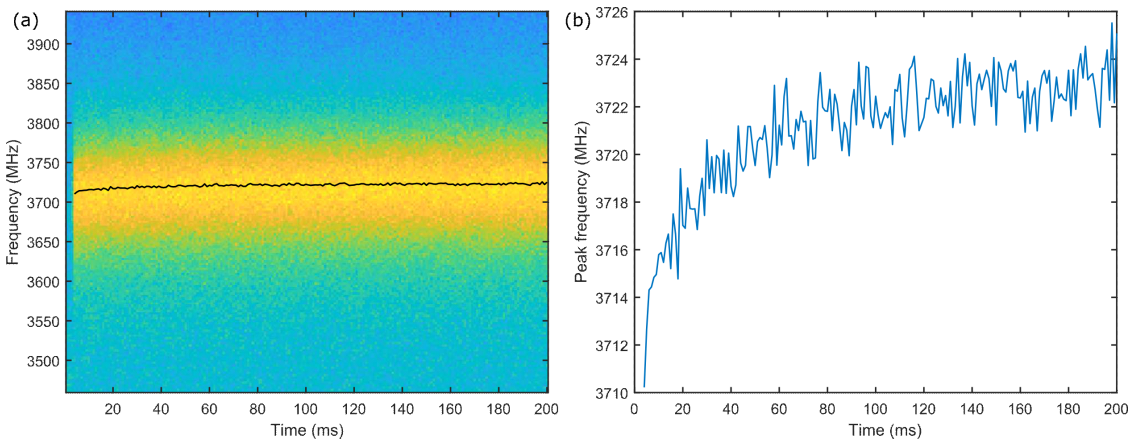

Fig. S5: Laser heating dynamics. (a) The Brillouin spectrum was measured in water with 338 mW laser power as the shutter was opened. Prior to recording the shutter is closed, so there is no laser power in the sample. The digital signal to open the shutter was sent at time = 0, and the spectrum measured with 1 ms dwell time for 200 ms. To provide high sensitivity at such short time window, the measurement was repeated 500 times and the spectra averaged over the repetitions. No Brillouin signal is visible in the first 3 ms, consistent with the specified time it takes the shutter to respond. Once open, the Brillouin peak shows minimal variation in time. (b) The fitted peak frequency over time, which indicates the local temperature at the focus. Laser heating results in a total of 58 MHz shift at this power (see Fig. S4a). Even at the first measurable point (4 ms), the frequency is close to its final stable value, with 77% of the total heating induced shift already present. Heating appears to be fully complete within 100ms, with no further shifts due to heating after the shutter has been open for 100ms.

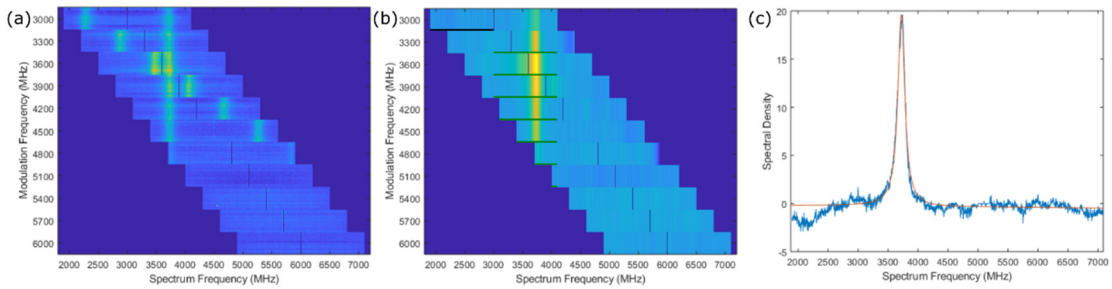

Fig. S6: Measurement of a Brillouin spectrum over a wide frequency range by scanning of the reference frequency. (a) A heatmap of individual spectra, shown both above and below the modulation frequency on the reference field. Detection frequencies below 6.25 MHz are excluded due to excess noise. An averaged spectrum is constructed for each reference frequency which is the median of each measurement at that frequency. (b) For each reference frequency, the true spectrum is estimated both above and below the reference as the median of data at every other frequency. This is highlighted for the 3000 MHz reference frequency, where the true spectrum above the reference frequency is estimated as the median value of the measured data at the green bars. This is then subtracted from the spectral range below the reference frequency (black bar). A similar process is applied both above and below each reference frequency to remove all spurious spectral features from the measured data. (c) The full spectrum is then estimated as the median value for each of the processed spectra as shown in (b).

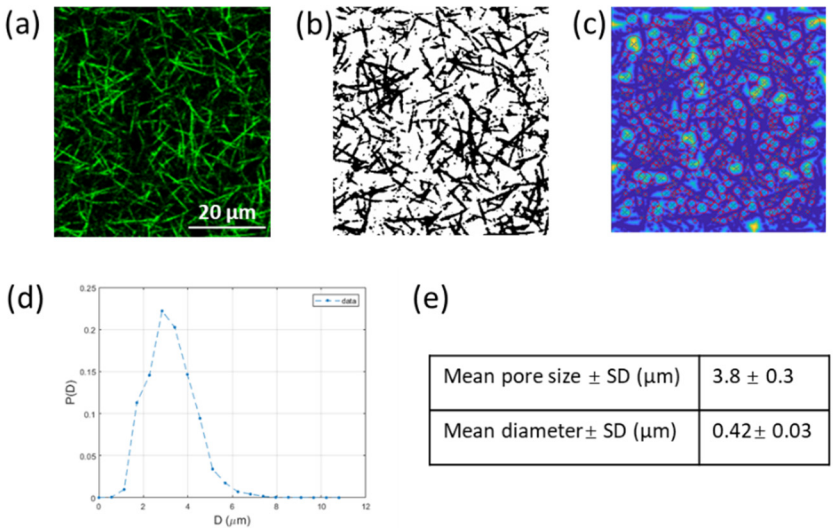

Mean pore size ± SD (µm)	3.8 ± 0.3
Mean diameter± SD (µm)	0.42± 0.03

Fig. S7: Fibrin hydrogel imaging and structural quantification for a sample prepared identically to the hydrogel shown in Fig. 3 of the main text. The fibrin hydrogel was polymerized at 37 °C using 4 mg/mL fibrinogen purified from pooled human plasma. (a) 3D Confocal reflectance microscopy imaging (Ex: 576 nm) performed 2 hours after the network formed. (b-e) Analysis of pore size and fiber diameter was performed as described in [1]. (b) Confocal images were then binarized. (c) The distance to the nearest fiber was estimated, and pores allocated to local maxima. (d) The distribution of pore sizes. (e) The mean and standard deviation of estimated pore size and fiber diameters.

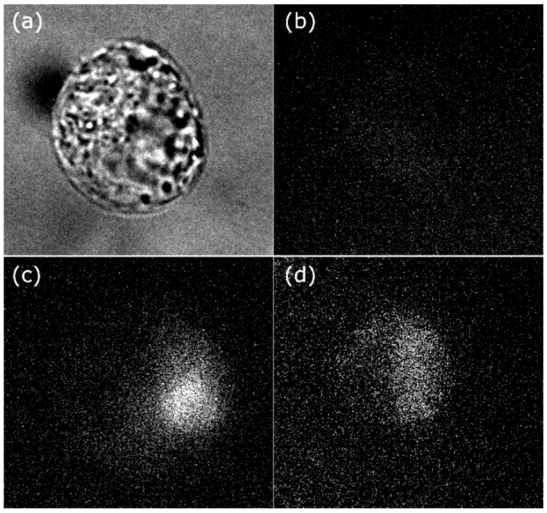

Fig. S8: Viability of HeLa cells after Brillouin image acquisition. (a) A brightfield image of the HeLa cell shown in Fig. 3 of the main text. (b) NucGreen live/dead stain (ThermoFisher) signal for the cell in (a) after acquisition of Brillouin images. This is imaged using widefield epifluorescence with a GFP filter set. (c) and (d), representative positive controls, where cells have been chemically damaged by addition of ethanol to induce death after imaging. Due to sample movement when adding the ethanol, the cell shown in (a) was not located for imaging after chemical damage.

Note 1: Experimental setup

Probe field:

The laser source is a low noise 1064 nm fiber laser with an output of up to 1 W (Azur Light ALS-IR-1064-1-I-SF-C). The sample is illuminated by a probe field, which is switched on or off using a digitally controlled shutter (Thorlabs SHB025T). The focal spot is scanned in 2D using galvo mirrors (Thorlabs GVS012) that are mapped to the back-focal plane of the objective using an F-theta scan lens (Thorlabs FTH160-1064-M39) and a tube lens (Thorlabs TTL200-B) which are aligned for telecentric beam scanning. Most Brillouin microscopes have used stage scanning, which has the advantage of enabling higher collection efficiency of the scattered signal, however use of galvanometric scanners was chosen here as it allows the sample to be kept static, alleviating any mechanical interference caused by moving the sample. The microscope objective (Nikon CFI Apo 60×W NIR N.A. 1.0) is positioned in Z with around 100nm resolution using a motorized stage (Thorlabs ZFM2020). The objective is under-filled at the back-focal plane to reduce its effective numerical aperture

Signal field:

Backscattered light is separated into the signal port using a quarter waveplate and a polarizing beamsplitter. Light which traverses the quarter waveplate twice, when travelling both forward and back again, experiences a half wave phase delay along the slow axis, which rotates linearly polarized light. The signal field is then collected into a single mode fiber with a collimation lens (Thorlabs F240APC-1064) that is confocally aligned with the laser focus. This signal field is then mixed with the reference field at a 50:50 splitter, with the resulting interference detected on a 1000 MHz bandwidth detector (Thorlabs PDB481C).

Reference field:

The reference field is produced using an optical fiber-based amplitude modulator (iXblue NIR-MX-LN-10) with a bias input set for dual sideband and carrier suppression, which means maximizing power in the frequency shifted sidebands while minimizing power in the unmodulated laser frequency. We detect 400 nW of unmodulated light when the modulation is left off, which is 4000 times less than the 1.6mW reference power used in experiments. To modulate the light we use an RF source (Aim-TTi TGR6000), with the output amplified (iXblue DR-AN-10-MO) and passed through a 1700 MHz high pass filter (Minicircuits VHF-1320+) before inputting to the amplitude modulator. The high pass filter is necessary to remove excess noise and achieve shot noise limited performance. The amplifier has an analog input which provides fine control of the gain, which we use to control and actively stabilize the total reference power reaching the detector. The use of a frequency shifted reference allows the detection bandwidth to be shifted to any frequency in the Brillouin scattering spectrum, limited only by the achievable modulation frequency.

Spectrum analysis:

The detector output signal is passed through a 1000 MHz low pass filter (Minicircuits SLP-1200+) to eliminate any residual signal at the modulation frequency, and then converted to a digital power spectrum using a custom-built real-time spectrum analyser in a National Instruments PXI system. This spectrum analyzer consists of a 3.2 GS/s digitizer (NI PXIe-5775) with an onboard FPGA running custom written LabVIEW FPGA code that converts the input to power spectra using a Fast Fourier Transform (FFT), and averages data to a single spectrum for a user defined duration. This onboard preprocessing is necessary for the function of the microscope, as the raw data is acquired at a rate of 4.2 GB/s. The averaged spectrum is transferred to the host computer and streamed to disk using a LabVIEW program that also controls the microscope hardware via analog, digital and serial outputs. The system can acquire and stream data continuously, with pauses in the acquisition due to computational processing accounting for less than 1% the acquisition time.

Table 1. Components in the PXI based spectrum analyzer

Item	NI Part number	Description
Chassis	PXIe-1092	Supports high speed data transfer from the digitizer to the host PC

Controller	PXIe-8880	Host PC running Windows 10, where data is streamed to disk and analyzed
Digitizer/FPGA	PXIe-5775	FlexRIO Digitizer with 3.2 GS/s 12-bit, and KU040 FPGA where spectrum analysis is performed
Data Acquisition Card	PXIe-6363	X Series DAQ (32 AI, 48 DIO, 4 AO), used to control the galvo scanners and other microscope parts

Parameter estimation:

The Brillouin shift ν and linewidth Γ were estimated for each measured spectrum using a custom script in Matlab 2019.

At the start of each measurement a baseline was recorded with the shutter closed to block the probe field. The first step in processing the measured spectra was to subtract the baseline from it. Then the level of excess shot noise from stray light was estimated and subtracted off for each measured spectrum. The remaining spectral values typically included only the Brillouin scattering peak, though in some instances residual noise would remain. The Brillouin peak would be estimated by least squares curve fitting a Lorentzian curve to the data. To minimize the effects of residual noise the fitting range would exclude detection frequencies with high noise, which were typically those below 100 MHz, and above 1000 MHz which falls outside the specifications of the detector.

Note 2: Shot noise limit

The shot noise limit to heterodyne detection is well established (e.g. see [2, 3]), and is reproduced here for the case with amplitude modulated reference field and unwanted background. The heterodyne measurement combines reference E_R and signal E_s fields on a 50/50 splitter, with two outputs;

$$E_1 = 2^{-\frac{1}{2}}E_R + 2^{-\frac{1}{2}}E_s \tag{1}$$

$$E_2 = 2^{-\frac{1}{2}}E_R - 2^{-\frac{1}{2}}E_s \tag{2}$$

In practice the signal field includes background scattering E_b from the sample. To simplify we separate the mean and fluctuations of the fields as

$$E_R = \bar{E}_R\left(e^{i(\omega_L-\Omega)t} + e^{i(\omega_L+\Omega)t}\right) + \delta E_R \tag{3}$$

$$E_s = \bar{E}_s\left(e^{i(\omega_L-\omega_B)t} + e^{i(\omega_L+\omega_B)t}\right) + E_b + \delta E_s \tag{4}$$

Here ω_L is the optical frequency, Ω the modulation frequency, ω_B the Brillouin scattering frequency, E_b the background scatter from the sample, and $\bar{E}_R$ and $\bar{E}_s$ are the average reference and signal amplitudes which we set to be real without loss of generality. We consider the reference to be bright and fluctuations small, so that $\bar{E}_R \gg \bar{E}_s, \delta E_R, \delta E_s$. The resulting subtraction photocurrent is given as

$$i = |E_1|^2 - |E_2|^2 \approx 2\bar{E}_R\bar{E}_s\cos(\Omega - \omega_B)t + 2\bar{E}_R Re\{E_b\} + 2\bar{E}_R Re\{\delta E_s\} + 2Re\{E_b\delta E_R\} \tag{5}$$

Here the small terms $\bar{E}_s\delta E_R$ and $\delta E_R\delta E_s$ have been neglected. The Brillouin signal is detected at the frequency $\omega = |\Omega - \omega_B|$, and as such it is ambiguous whether the Brillouin frequency corresponds to $\omega_B = \Omega - \omega$ or $\omega_B = \Omega + \omega$. This ambiguity can be resolved by scanning the modulation Ω (as shown in Fig. S6).

To estimate the signal, we extract the photocurrent at frequency $\omega = |\Omega - \omega_B|$, which provides:

$$i(\omega) = \bar{E}_R\bar{E}_s + \bar{E}_R\xi_S + E_b\xi_R \tag{6}$$

Here we have defined $\xi_S = Re\{\delta E_s(\omega)\}$, $\xi_R = Re\{\delta E_R(\omega)\}$, which at the shot noise limit have the properties $\langle\xi\rangle = 0$, and $\langle\xi^2\rangle = 1$. The fixed variance corresponds to zero point fluctuations of the electromagnetic field [3]. An estimate of $i(\omega)$ then has variance of $\Delta i^2(\omega) = \langle i^2(\omega)\rangle - \langle i(\omega)\rangle^2$, with

$$\langle i^2(\omega)\rangle = n_R n_s + n_R\langle \xi_S^2\rangle + n_b\langle \xi_R^2\rangle \tag{7}$$

$$\langle i(\omega)\rangle^2 = n_R n_s \tag{8}$$

Here $n_R = \bar{E}_R^2$, $n_s = \bar{E}_s^2$, and $n_b = E_b^2$ are mean photon numbers in the reference, signal, and background fields respectively. At the shot noise limit we find the signal to noise ratio (SNR) of an estimate of $i(\omega)$ is given by

$$\mathrm{SNR}_i = \frac{\langle i(\omega)\rangle^2}{\Delta i^2(\omega)} = \frac{n_s n_R}{n_R + n_b} \approx n_s \tag{9}$$

The approximation is valid provided $n_R \gg n_b$, as is typically true. This SNR is the most commonly considered shot noise limit. The Brillouin peak, however, is estimated based on spectral power, which we define as

$$S = i(\omega)^2 = n_R n_s + n_R\xi_S^2 + n_b\xi_R^2 + 2n_R\bar{E}_s\xi_S + 2\bar{E}_R\bar{E}_s E_b\xi_R + 2\bar{E}_R E_b\xi_S\xi_R \tag{10}$$

$$\langle S\rangle^2 = n_R^2 n_s^2 + n_R^2\langle\xi_S^2\rangle^2 + n_b^2\langle\xi_R^2\rangle^2 + 2n_R^2 n_s\langle\xi_S^2\rangle + 2n_R n_s n_b\langle\xi_R^2\rangle + 2n_R n_b\langle\xi_S^2\rangle\langle\xi_R^2\rangle \tag{11}$$

$$\langle S^2\rangle = n_R^2 n_s^2 + n_R^2\langle\xi_S^4\rangle + n_b^2\langle\xi_R^4\rangle + 6n_R^2 n_s\langle\xi_S^2\rangle + 6n_R n_s n_b\langle\xi_R^2\rangle + 6n_R n_b\langle\xi_S^2\rangle\langle\xi_R^2\rangle \tag{12}$$

Here we have used $\langle\xi\rangle = \langle\xi^3\rangle = 0$. This leads to

$$\Delta^2 S = n_R^2(\langle\xi_S^4\rangle - \langle\xi_S^2\rangle^2) + n_b^2(\langle\xi_R^4\rangle - \langle\xi_R^2\rangle^2) + 4n_R^2 n_s\langle\xi_S^2\rangle + 4n_R n_s n_b\langle\xi_S^2\rangle + 4n_R n_b\langle\xi_S^2\rangle\langle\xi_R^2\rangle \tag{13}$$

Since ξ is a Gaussian variable, $(\langle\xi^4\rangle - \langle\xi^2\rangle^2) = 2\langle\xi^2\rangle^2 = 2$, and

$$\Delta^2 S = 2n_R^2 + 2n_b^2 + 4n_R^2 n_s + 4n_R n_s n_b + 4n_R n_b \tag{14}$$

As such the shot noise limit for an estimate of spectral power is given as

$$\mathrm{SNR}_S = \frac{\langle S - n_R - n_b\rangle^2}{\Delta S^2} = \frac{n_s^2 n_R^2}{2n_R^2 + 2n_b^2 + 4n_R^2 n_s + 4n_R n_s n_b + 4n_R n_b} \approx \frac{n_s^2}{4n_s + 2} \tag{15}$$

Here the constant shot noise floor $n_R + n_b$ is subtracted from S as it is independent of the signal spectrum we aim to measure. The final approximation uses $n_R \gg n_b, n_S$, and is valid for the experimental conditions. Experiments use 1.6mW of detected reference power, so detection of 20μW of background, for instance, corresponds to $n_b \approx 0.0125\, n_R$, which increases the noise by a factor of 1.025, and reduces the SNR by a factor of 0.976. For the current experiments, this can be considered negligible. This SNR asymptotes to photon counting performance at large photon number, but incurs a constant noise penalty that is deleterious for $n_s \ll 1$.

Note 3: Cramér–Rao bound on Brillouin frequency estimation

The Cramér–Rao bound establishes the limit to estimation of a parameter with stochastic data, limited by the Fisher Information [4] which for estimation of a single parameter is defined as

$$I(\theta) = \int \left(\frac{\partial}{\partial\theta}\log P(X;\theta)\right)^2 P(X;\theta)\, dx \tag{16}$$

Here P is the probability density of the measurement outcome X given the true value of the parameter θ to be estimated. Here I am considering the measured parameter X to be spectral power at each frequency. Because the spectra are heavily averaged, the probability distribution is very well approximated as a normal distribution, with probability at each frequency component given by

$$P_\omega(X) = \frac{1}{\sqrt{2\pi}\,\sigma}\, e^{-\frac{\frac{1}{2}(X-\bar{X})^2}{\sigma^2}} \tag{17}$$

To find information for any parameter θ, note the following

$$\frac{\partial}{\partial\theta}\log P_\omega(X;\theta) = \frac{\partial\bar{X}}{\partial\theta}\frac{\partial}{\partial\bar{X}}\log P_\omega = \frac{\partial\bar{X}}{\partial\theta}\frac{X-\bar{X}}{\sigma^2} \tag{18}$$

Using Eq. (18) and Eq. (16)

$$I(\theta) = \left(\frac{\partial\bar{X}}{\partial\theta}\right)^2 \frac{1}{\sqrt{2\pi}\,\sigma}\int\left(\frac{X-\bar{X}}{\sigma^2}\right)^2 e^{-\frac{\frac{1}{2}(X-\bar{X})^2}{\sigma^2}}\,dX$$

$$= \left(\frac{\partial\bar{X}}{\partial\theta}\right)^2 \frac{1}{\sqrt{2\pi}\,\sigma}\int\left(\frac{X}{\sigma^2}\right)^2 e^{-\frac{\frac{1}{2}(X)^2}{\sigma^2}}\,dX = \left(\frac{\partial\bar{X}}{\partial\theta}\right)^2 \sigma^{-2}. \tag{19}$$

This provides the unsurprising conclusion that estimation has a minimum uncertainty of

$$\Delta\theta \geq \sigma \Big/ \left|\frac{\partial\bar{X}}{\partial\theta}\right|. \tag{20}$$

Here we estimate a Brillouin scattering spectral peak, with $X = S(\omega) - n_R$ representing the measured spectral power, $\bar{X} = n_R n_s(\omega)$ the true average spectrum, and as discussed above $\sigma^2 = n_R^2(4n_s(\omega)+2)$. Here we consider a resonant peak with a signal spectrum of

$$n_s(\omega) = \frac{n_T\Delta\omega\gamma/\pi}{\gamma^2 + (\omega-\omega_0)^2} \tag{21}$$

Here n_T is the total photon number in the peak, and $\Delta\omega$ is the increment between frequencies in the Fourier transform. The photon number is normalized using the approximation

$$n_T = \sum_\omega n_s(\omega) \approx \frac{1}{\Delta\omega}\int n_s(\omega)\,d\omega \tag{22}$$

This is valid provided the frequency increment is much smaller than the spectral linewidth γ. The duration of each individual measurement defines $\frac{1}{\Delta\omega}$, with longer duration measurements increasing the number of frequencies represented in the Fourier domain and thereby the photon number, though SNR is unchanged at each individual frequency. When estimating the peak frequency, we substitute $\theta = \omega_0$ into Eq. (19), which requires the following function

$$\frac{\partial\bar{X}}{\partial\omega_0} = \frac{2n_T\Delta\omega\,\gamma\,\overline{n_R}\,(\omega-\omega_0)}{\pi(\gamma^2+(\omega-\omega_0)^2)^2} \tag{23}$$

To estimate the central frequency of the peak we add together the information derived from all the different measured frequencies.

$$I(\omega_0) = \sum_{\omega_1}^{\omega_N} I_\omega = \sum_{\omega_1}^{\omega_N}\left(\frac{\partial\bar{X}(\omega)}{\partial\omega_0}\right)^2\sigma^{-2} \approx \frac{1}{\Delta\omega}\int_{-\infty}^{\infty}\left(\frac{\partial\bar{X}(\omega)}{\partial\omega_0}\right)^2\sigma^{-2}\,d\omega \tag{24}$$

The replacement of the finite sum with an integral is valid provided the bandwidth of the measurement is large enough to encompass all the available information. The equation is difficult to solve using the exact measurement variance from Eq. (14), $\sigma^2 = n_R^2(4n_s(\omega)+2)$. However it is easily solvable in the limits of high photon number $n_s(\omega) \gg 1$ and low photon number $n_s(\omega) \ll 1$. In the limit of large photon number, we have $\sigma^2 \approx 4n_R^2 n_s(\omega)$ and the Fisher information is

$$I(\omega_0) = \frac{1}{\Delta\omega}\int_{-\infty}^{\infty}\left(\frac{2\,n_T\Delta\omega\,\gamma\,\overline{n_R}\,(\omega-\omega_0)}{\pi(\gamma^2+(\omega-\omega_0)^2)^2}\right)^2 \frac{\gamma^2+(\omega-\omega_0)^2}{4\overline{n_R}^2\,n_T\Delta\omega\,\gamma/\pi}d\omega$$

$$= \frac{n_T\,\gamma}{\pi}\int_{-\infty}^{\infty}\frac{\omega^2}{(\gamma^2+\ \omega^2)^3}\,d\omega = \frac{n_T}{8\,\gamma^2} \tag{25}$$

As such the minimum resolvable frequency shift is

$$\Delta\omega_0^2 \geq \frac{8\,\gamma^2}{n_T} \tag{26}$$

This is similar to the sensitivity achievable with photon counting detectors (derived below). In the limit of small photon number, we have $\sigma^2 \approx 2n_R^2$ and the Fisher information is instead given by

$$I(\omega_0) = \frac{1}{\Delta\omega}\int_{-\infty}^{\infty}\left(\frac{2\,n_T\Delta\omega\,\gamma\,\overline{n_R}\,(\omega-\omega_0)}{\pi(\gamma^2+(\omega-\omega_0)^2)^2}\right)^2\frac{1}{2\,\overline{n_R}^2}\,d\omega = \frac{\Delta\omega\,n_T^2}{4\pi\,\gamma^3} \tag{27}$$

Such that the minimum resolvable frequency shift is

$$\Delta\omega_0^2 \geq \frac{4\pi\gamma^3}{\Delta\omega\,n_T^2} = \frac{2\gamma^3}{P_T^2 T} \tag{28}$$

With P_T the total signal photon flux/second, and T the total averaging time. The second expression has some practical value; it is equally applicable both to increased measurement duration via longer acquisition, which leads to narrower bandwidth narrower bandwidth $\Delta\omega$, and when averaging many measurements. In both cases the increase in total duration provides the same linear decrease in noise variance. At fixed total averaging time T, changing the frequency resolution $\Delta\omega$ has no effect on the precision. The dependence of $\Delta\omega_0 \propto P_T^{-1}$ and $\Delta\omega_0 \propto T^{-1/2}$ are shown experimentally in Fig S3.

When compared to the expression at high photon number, we see that this uncertainty is larger by a factor of $\frac{\pi\gamma}{2\Delta\omega n_T} = \frac{1}{4n_\tau}$, where n_τ is the mean number of signal photons collected in the scattering coherence time of $\tau = 1/\gamma$. This shows that the noise penalty in heterodyne is relevant when fewer than 1 photon is collected within the coherence time.

To provide a more experimentally applicable expression, we can parametrize the achievable precision in terms of the peak signal-to-noise ratio (SNR_p), defined as the squared amplitude of the Brillouin peak $S(\omega_0)^2$ divided by the background spectrum variance $\sigma^2 \approx 2n_R^2$. Using Eq. (15) and Eq. (21), the SNR_p can be expressed as a function of photon numbers as

$$\mathrm{SNR}_p \approx \frac{n_s^2(\omega_0)}{2} = \frac{n_T^2\Delta\omega^2}{2\pi^2\gamma^2} \tag{29}$$

Using this in Eq. (28), we find

$$\Delta\omega_0^2 \geq \frac{2\gamma\Delta\omega}{\pi\,\mathrm{SNR}_p} \tag{30}$$

Photon counting Cramér–Rao bound

Here we perform a similar analysis of the Cramér–Rao bound to the case of a spectrometer using photon counting. In this case the measured parameter X a photon number at each frequency, which must be discreet number. Photon numbers follow a Poisson distribution:

$$P_\omega(X;\mu) = \frac{\mu^X e^{-\mu}}{X!} \tag{31}$$

Here μ is the mean photon number. The Fisher information is given by

$$I(\theta) = \left(\frac{\partial \mu}{\partial \theta}\right)^2 E\left[\left(\frac{\partial}{\partial \mu}\log P_\omega\right)^2\right] = \left(\frac{\partial \mu}{\partial \theta}\right)^2 \frac{1}{\mu} \tag{32}$$

Where $E[\ ]$ denotes the expectation value. Comparing Eq. (32) to the equivalent Eq. (19) derived for Gaussian statistics, we see that here σ^2 has been replaced with μ. This is unsurprising given that the distribution variance is equal to μ. Similar to the above, we use

$$\mu(\omega) = \frac{n_T \Delta\omega\gamma/\,\pi}{\gamma^2 + (\omega - \omega_0)^2} \tag{33}$$

$$\frac{\partial \mu}{\partial \omega_0} = \frac{2\, n_T \Delta\omega\, \gamma\, (\omega - \omega_0)}{\pi(\gamma^2 + (\omega - \omega_0)^2)^2} \tag{34}$$

To estimate change in central frequency we again add together the information derived from all the measured frequencies.

$$I(\omega_0) = \frac{1}{\Delta\omega}\int_{-\infty}^{\infty}\left(\frac{\partial \mu}{\partial \omega_0}\right)^2 \mu^{-1}\, d\omega = \frac{4\, n_T\, \gamma}{\pi}\int_{-\infty}^{\infty}\frac{\omega^2}{(\gamma^2+(\omega-\omega_0)^2)^3}\, d\omega = \frac{n_T}{2\,\gamma^2} \tag{35}$$

Hence, we find that the Poissonian statistics achieve slightly higher precision than Eq. (26) for heterodyne at high signal power

$$\Delta\omega_0^2 \geq \frac{2\,\gamma^2}{n_T} \tag{36}$$

Note 4: Calibration materials

Figure 2 of the main text shows Brillouin spectra measured for methanol, ethanol, isopropanol, acetone and water, with measured Brillouin shifts compared to expected values. In each case the expected Brillouin frequency was calculated as

$$\nu = \frac{2c_s}{n\lambda} \tag{37}$$

Here n is the refractive index, c_s the speed of sound in the liquid, and λ the vacuum wavelength. The speed of sound for each liquid was taken from the Dortmund Data Bank [5], and the refractive index from the Refractive index database [6]. As shown above in Fig. S4, the laser can induce sample heating. The amount of heating will depends on both the thermal conductivity and the optical absorption of the materials [7]. We were unable to find this information for all materials, and so assumed a similar temperature to water, instead of attempting to infer the different rates of heating with insufficient information. All measurements were taken at room temperature (22 °C) with the laser heating assumed to be approximately 8K, such that the assumed temperature was 303.15K (30 °C). The measured and expected shifts closely align, with some small deviations. The deviations could be due to differences in temperature from the assumed value.

The Brillouin linewidth was also measured and shown to correlate approximately with the kinematic viscosity, which is a rheological parameter measured at low frequencies (Fig. 2d). We did not predict the expected Brillouin linewidth as it depends on both the shear (kinematic) and bulk viscosities, as well as the heat transport coefficient [8]. We were unable to find values for the bulk viscosities for all of the materials. We instead plot the Brillouin linewidth against the kinematic viscosity at the assumed temperature of 303.15K [9]. The kinematic viscosity contributes to the broadening of the Brillouin linewidth, and hence we expected the trend of increasing Brillouin linewidth at increasing kinematic viscosity (Fig. 2d). While this is suggestive that the Brillouin linewidth increases

with increasing kinematic viscosity, this is only a general trend, and it is not generally possible to estimate kinematic viscosity from Brillouin linewidth because of the additional contribution of bulk viscosity.

References

1. M. Molteni, D. Magatti, B. Cardinali, M. Rocco, and F. Ferri, "Fast Two-Dimensional Bubble Analysis of Biopolymer Filamentous Networks Pore Size from Confocal Microscopy Thin Data Stacks," Biophysical Journal **104**, 1160-1169 (2013).
2. H. P. Yuen and V. W. Chan, "Noise in homodyne and heterodyne detection," Opt. Lett. **8**, 177-179 (1983).
3. W. P. Bowen and G. J. Milburn, *Quantum optomechanics* (CRC Press, 2015).
4. A. Van den Bos, *Parameter estimation for scientists and engineers* (John Wiley & Sons, 2007).
5. "Dortmund Data Bank (DDB), DDBST GmbH ", retrieved 08/2021, http://www.ddbst.com/.
6. "Refractive index database", retrieved 08/2021, https://refractiveindex.info/.
7. E. J. Peterman, F. Gittes, and C. F. Schmidt, "Laser-induced heating in optical traps," Biophys. J. **84**, 1308-1316 (2003).
8. J. Rouch, C. Lai, and S. Chen, "Brillouin scattering studies of normal and supercooled water," J. Chem. Phys. **65**, 4016-4021 (1976).
9. D. S. Viswanath, T. K. Ghosh, D. H. Prasad, N. V. Dutt, and K. Y. Rani, *Viscosity of liquids: theory, estimation, experiment, and data* (Springer Science & Business Media, 2007).